The Lyman α forest power spectrum from the XQ-100 Legacy Survey

Vid Iršič,[1,2]★ Matteo Viel,[3,4,5]★ Trystyn A. M. Berg,[6] Valentina D'Odorico,[3]
Martin G. Haehnelt,[7] Stefano Cristiani,[3,5] Guido Cupani,[3] Tae-Sun Kim,[3]
Sebastian López,[8] Sara Ellison,[6] George D. Becker,[7,9] Lise Christensen,[10]
Kelly D. Denney,[11] Gábor Worseck[12] and James S. Bolton[13]

[1]*The Abdus Salam International Centre for Theoretical Physics, Strada Costiera 11, I-34151 Trieste, Italy*
[2]*Department of Astronomy, University of Washington, 3910 15th Ave NE, WA 98195-1580 Seattle, USA*
[3]*INAF – Osservatorio Astronomico di Trieste, Via G. B. Tiepolo 11, I-34143 Trieste, Italy*
[4] *SISSA – International School for Advanced Studies, Via Bonomea 265, I-34136 Trieste, Italy*
[5]*INFN – National Institute for Nuclear Physics, via Valerio 2, I-34127 Trieste, Italy*
[6]*Department of Physics and Astronomy, University of Victoria, Victoria, BC V8P 1A1, Canada*
[7]*Institute of Astronomy and Kavli Institute of Cosmology, Madingley Road, Cambridge CB3 0HA, UK*
[8]*Departamento de Astronomía, Universidad de Chile, Casilla 36-D, Santiago, Chile*
[9]*Space Telescope Science Institute, 3700 San Martin Drive, Baltimore, MD 21218, USA*
[10]*Dark Cosmology Centre, Niels Bohr Institute, University of Copenhagen, Juliane Maries Vej 30, DK-2100 Copenhagen, Denmark*
[11]*Department of Astronomy, The Ohio State University, 140 West 18th Avenue, Columbus, OH 43210, USA*
[12]*Max-Planck-Institut für Astronomie, Königstuhl 17, D-69117 Heidelberg, Germany*
[13]*School of Physics and Astronomy, University of Nottingham, University Park, Nottingham NG7 2RD, UK*

ABSTRACT

We present the Lyman α flux power spectrum measurements of the XQ-100 sample of quasar spectra obtained in the context of the European Southern Observatory Large Programme 'Quasars and their absorption lines: a legacy survey of the high redshift universe with VLT/XSHOOTER'. Using 100 quasar spectra with medium resolution and signal-to-noise ratio, we measure the power spectrum over a range of redshifts $z = 3$–4.2 and over a range of scales $k = 0.003$–$0.06 \, \mathrm{km}^{-1}$ s. The results agree well with the measurements of the one-dimensional power spectrum found in the literature. The data analysis used in this paper is based on the Fourier transform and has been tested on synthetic data. Systematic and statistical uncertainties of our measurements are estimated, with a total error (statistical and systematic) comparable to the one of the BOSS data in the overlapping range of scales, and smaller by more than 50 per cent for higher redshift bins ($z > 3.6$) and small scales ($k > 0.01 \, \mathrm{km}^{-1}$ s). The XQ-100 data set has the unique feature of having signal-to-noise ratios and resolution intermediate between the two data sets that are typically used to perform cosmological studies, i.e. BOSS and high-resolution spectra (e.g. UVES/VLT or HIRES). More importantly, the measured flux power spectra span the high-redshift regime that is usually more constraining for structure formation models.

Key words: methods: data analysis – intergalactic medium – cosmology: observations – large-scale structure of Universe.

1 INTRODUCTION

The absorption features bluewards of the Lyman α (Lyα) emission line in the spectra of high-redshift quasars (QSOs) are widely used as biased tracers of the density fluctuations of a photoionized warm intergalactic medium (IGM), and are collectively known as the Lyα forest (see Meiksin 2009; McQuinn 2016 for recent reviews).

Although the first speculations and measurements were made almost 50 yr ago (Gunn & Peterson 1965; Lynds 1971), the physical picture of the Lyα forest was established in the 1990s by a detailed comparison of analytic calculations (Bi & Davidsen 1997; Hui 1999; Viel et al. 2002) and numerical simulations (Cen et al. 1994; Zhang, Anninos & Norman 1995; Hernquist et al. 1996; Miralda-Escudé et al. 1996; Theuns et al. 1998, 2002) with observed absorption spectra (e.g. Kim et al. 2004).

In the last decade, a range of different statistics have been proposed (Ricotti, Gnedin & Shull 2000; Schaye et al. 2000; Theuns &

★ E-mail: irsic@uw.edu (VI); viel@sissa.it (MV)

Zaroubi 2000; Theuns et al. 2002; Viel et al. 2005; Bolton et al. 2008; Lidz et al. 2010; Becker et al. 2011; Bolton et al. 2012; Garzilli et al. 2012; Rudie, Steidel & Pettini 2012; Iršič et al. 2013; Boera et al. 2014; Lee et al. 2015), and successfully used, that focused on specific aspects (e.g. targeting cosmology, temperature of the IGM, etc.). However, the main quantity of choice when comparing observations with the theoretical predictions has become the one-dimensional flux power spectrum $P_F(k)$ (Croft et al. 1999, 2002; Kim et al. 2004; Viel, Haehnelt & Springel 2004; McDonald et al. 2005; Palanque-Delabrouille et al. 2013; Viel et al. 2013a). This is because the flux power spectrum is tracing the actual fluctuations in the observed forest, making it easy to understand systematics and the noise properties. The flux power spectrum also more cleanly decouples the scales involved (e.g. fluctuations due to poor continuum fitting are restricted to large scales).

Several measurements of the flux power spectrum have been performed in the last two decades, ranging from measurements on a few 10 high-resolution, high signal-to-noise ratio QSO spectra (Vogt et al. 1994; Kim et al. 2004; Viel et al. 2004, 2013a) to measurements on many thousands of QSO spectra with poor resolution and signal to noise (York et al. 2000; McDonald et al. 2005; Dawson et al. 2013; Palanque-Delabrouille et al. 2013). Taken together, these measurements cover over three orders of magnitude in scale ($k = 0.001$–0.1 km^{-1} s); however, they are either only centred on large scales, or only on small scales, and no study has done a combined measurements of both.

In this paper, we present a new set of measurements of the one-dimensional $P_F(k)$ on an intermediate data set: a hundred QSO spectra with medium resolution ($\sim$10–20 km s^{-1}) and medium signal-to-noise ratio ($S/N \sim$ 10–30). The goal is to achieve measurements of both large and small scales simultaneously and thus provide a bridge between the traditionally used data sets probing either large or small scales.

The paper is structured as follows: in Section 2, we discuss the observational data used in our analysis, as well as the synthetic data on which the data analysis procedure was tested. The various steps of the data analysis are described in detail in Section 3. The final results are presented in Section 4 and we conclude in Section 5.

2 DATA AND SYNTHETIC DATA

2.1 XQ-100 Sample

In this work, we use 100 QSO spectra from the XQ-100 Legacy Survey (López et al. 2016), observed with the X-Shooter spectrograph on the Very Large Telescope (Vernet et al. 2011). These 100 quasars span the redshift range $3.51 < z < 4.55$.

We limit ourselves to spectra obtained from the UVB and VIS spectrograph arms [see López et al. (2016) for more details], since the near-infrared spectral range gives us no information regarding the Lyα forest. For each QSO spectrum, we merge the two spectral arms into one spectrum by a simple method. We re-bin the spectra on to a fixed wavelength grid with $\Delta\log_{10}\lambda = 3 \times 10^{-5}$ (with λ in Å), which is the larger of the two bin sizes of the individual arms. In the region where the arms overlap, we perform weighted average of the flux, continuum and resolution element. We have performed a test where we treated each spectral arm as independent quasar observation and the results showed that the effect of simple merging has negligible effect on the flux power spectrum measurements, at least at the scales where we are able to measure it.

Since the weighting is done using the optimal inverse variance weights, any bad pixel that was determined to be so during
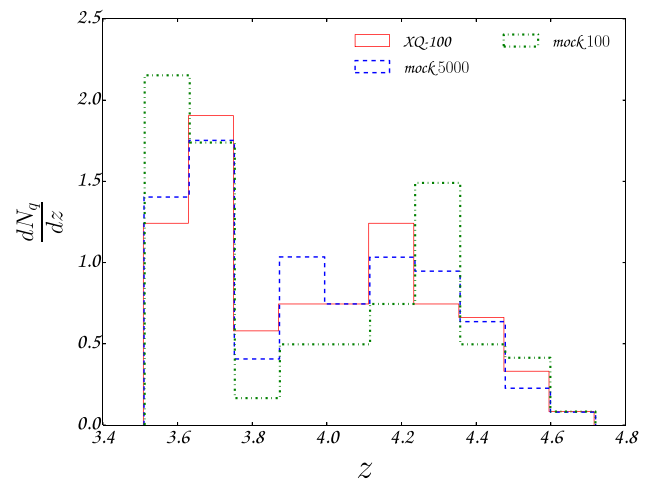

Figure 1. The QSO redshift distribution for XQ-100 data sample (red), for $N_Q = 5000$ quasars of the synthetic data sample (blue) and for $N_Q = 100$ quasars of a synthetic data sub-sample (green).

pipeline reduction analysis is thus down-weighted. However, the subsequent merged spectra are also examined by eye if they make sense and do not have any pixels that are obvious outliers. Using weighted merging of the arms also ensures that the continuum transition from one arm to the other is smooth. Whether this introduces some false large-scale fluctuations in the continuum was not thoroughly explored, however any such contributions would show up as excess of continuum power, which we have investigated and verified it is very small (comparable to the noise levels); see Section 4.5.

The resolution elements were taken to be constant per arm, with the values of 20 and 11 km s^{-1} for UVB and VIS arms, respectively.

The continuum used in our analysis is based on cubic spline fits and is described in more detail in López et al. (2016).

After the spectral arms have been merged, we perform additional cuts on the data. First, we exclude pixels with negative or zero flux errors as well as any bad pixels (with very negative flux of $f < -10^{-15}$, or as a flux over continuum level $f/C < -100$).

Secondly, we mask regions around Damped Lyman α (DLA) systems, using the DLA sample provided by the survey team (Sánchez-Ramírez et al. 2016). We do not use data within 1.5 equivalent widths from the centre of the DLA.

When measuring the flux power spectrum within the Lyα forest, we only use the pixels within the 1045–1185 Å restframe wavelength range of each QSO spectrum. This range is conservative in the sense that we do not probe the absorption region close to the quasar Lyα and Lyβ emission lines (McDonald et al. 2005).

2.2 Synthetic data

Our data analysis pipeline was tested with synthetic data that were generated exclusively for this work. We want to generate a realistic flux field with a QSO redshift distribution matching that of the observed data sample.

First, we approximated the observed QSO redshift distribution by binning the emission redshifts of the XQ-100 sample into 10 redshift bins, as shown in Fig. 1. To generate synthetic QSO sample, we have drawn their redshifts from this distribution. Fig. 1 shows the distribution of 5000 and 100 randomly drawn QSO redshifts from the distribution given by the data.

Table 1. Different mock catalogues used in testing the data-analysis routine.

Name	N_Q	Pixel size/resolution
mock 5000	5000	XQ-100 values
mock 100	100	XQ-100 values

The various mock QSO catalogues used in this paper are presented in Table 1.

In the next step, we want to produce flux spectra along the line of sight of each QSO from the synthetic catalogues. To this end, we use a suite of high-resolution hydro-dynamical simulations of the IGM between redshifts $3 < z < 5$, with 2×2048^3 particles in a $40\,h^{-1}$ Mpc box size (PRACE: Sherwood simulations – Bolton et al. 2017). The outputs were produced with a redshift step of $\Delta z = 0.1$ in a given redshift range, in the form of an extracted optical depth along 5000 randomly selected lines of sight.

For each line of sight, and each redshift bin, the simulated optical depth is given on a velocity grid ($\tau(v)$).

First, we convert this to a grid of wavelengths (λ), or equivalently Lyα absorption redshifts ($1 + z = \lambda/\lambda_\alpha$), where λ_α stands for Lyα line (1215.67 Å). The conversion is done so that the mean absorption is assumed to happen at the redshift bin of the simulation output (z_s)

$$\lambda = \lambda_\alpha \, (1 + z_s) \sqrt{\frac{1 + \frac{v}{c}}{1 - \frac{v}{c}}}, \tag{1}$$

where v is the velocity coordinate along the line of sight within a simulation box. Since the length of the absorption spectrum along each line of sight, at a given redshift z_s extends over the whole box size, and since the cosmological simulations have periodic boundary conditions, we make use of that to extend the signal also to negative velocities by periodically repeating the spectrum from a simulation box. Thus, for a redshift bin z_s, the signal spans the redshift range of $z_s - \Delta z_s < z < z_s + \Delta z_s$, where Δz_s is simply the redshift length of the simulation box at a redshift z_s. We choose to only repeat the periodic signal once, since in the case of our simulations the redshift difference between each z_s and its neighbours is less than $2\Delta z_s$.

Secondly, we collect all the redshift outputs along each line of sight into a single optical depth array. In principle, the merging of the simulation boxes at different redshifts can be done using a variety of methods (e.g. weighted interpolation between signals in neighbouring redshift bins). However, we adopted the simplest method and order them, one after the other, by increasing simulation redshift, choosing simulation redshift bin with lower mean redshift in the areas of overlap between two simulation outputs.

Such a construction allows us to have a line of sight extending over many redshifts, and thus mimicking the observed spectrum. There are, of course, a few shortcomings we would like to point out.

Most importantly, our basic ingredient is a spectrum extracted from a numerical simulation with a given box size. Hence, we will only be able to measure meaningful statistics on smaller scales. But we will be able to do so for each redshift along a single line of sight.

Secondly, such a construction has rather discrete jumps in flux on the border between regions from simulation outputs with different mean redshift. The artefacts in a spectrum caused by such discrete jumps can be avoided by using a more advanced technique of merging the simulation outputs together along each line of sight, such as linear (or higher order) interpolation. However, for our own tests

on the power spectrum, this did not play an important role, and thus we settled for the simplest merging.

Thirdly, it is usually common to rescale the optical depth acquired from simulations at a given redshift, so that the mean flux in that redshift bin matches the observed one. Such re-scaling can be viewed as a correction of the ultraviolet background ionization rate from the simulations to match the observed mean flux (due to degeneracy between the two). The increase (or decrease) in the optical depth is usually less than 20 per cent.

We performed a similar correction, but on the optical depth along the entire constructed line of sight. The correction factor had a redshift dependence, with redshift binning matching that of the simulation output. The values were computed through iteration with the condition that the mean flux computed along a specific line of sight matches one from observations. For the purpose of testing the data analysis on synthetic data, it did not matter what exactly is the input observed mean flux, as long as we recover it. We chose to use one given by Palanque-Delabrouille et al. (2013).

The last part in creating the synthetic data involved tailoring the simulation output to a given survey specifications: QSO redshift distribution, pixel-size, resolution and noise properties.

First, we assigned a QSO emission redshift to each line of sight, thus specifying what part of the redshift range falls in the Lyα forest region for that QSO spectrum. Quasars used in this procedure were determined by the synthetic quasar catalogue.

Each QSO spectrum was then rebinned with the same wavelength bin size as in the XQ-100 observations ($\Delta\log_{10}\lambda = 3 \times 10^{-5}$).

A convolution was performed on each spectrum with a Gaussian kernel with resolution element of $33\,\mathrm{km\,s^{-1}}$. Such a resolution element is larger than the one in XQ-100 survey but for our purposes of testing the data analysis procedure the exact number did not matter.

In the end, we also added noise to the spectrum. In principle, adding noise after the convolution with the resolution kernel only adds a component that is flux-independent (e.g. read-out noise). If the dominating contribution to the noise were flux dependent (e.g. Poisson noise), we could add it before convolving with the resolution kernel. Both options were tested in the synthetic data and subsequent data analysis, but for most of the tests presented in the rest of the paper synthetic data has only flux-independent noise component added.

To make sure that our data-analysis routines correctly recognize and subtract the noise, we used a noise model that is comparable to averaging the flux errors of the actual XQ-100 data. As shown in Fig. 2, the noise has a slight wavelength dependence towards the edges of the spectrum. Even though the scatter is not negligible, it was not modelled in the synthetic data. The function we used to describe the noise model in the synthetic data is not a fit to the averaged flux errors. It is just a simple closed form function that exhibits the same large-scale wavelength-dependence behaviour. We found that for testing purposes of this paper such a model was sufficient.

The very complicated flux error dependence comes from two instrumental effects. First is that the flux error has a long wavelength mode modulation, where it increases towards the edges of the observed spectral range, which coincides with the edges of the CCD camera where the pixel sensitivity is lower than that in the middle of the CCD. This is the effect we wanted to capture in the model of the flux errors since a large mode fluctuation in real space of the flux errors might cause sharp features in the Fourier space. We wanted to make sure we access such a possibility on the mock data, and understand any potential systematics it might cause. However, our error estimate did not show any weird behaviour compared to
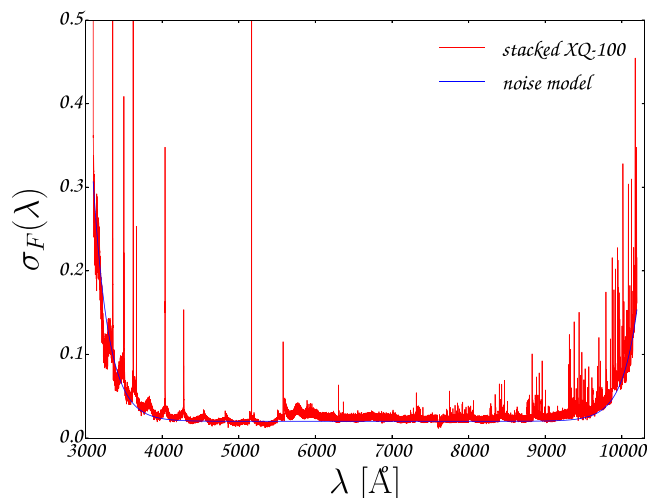
Figure 2. Averaged flux errors of the XQ-100 sample (in red) compared to the noise model used in constructing the synthetic spectra (in blue).

having a constant value of flux error with wavelength. Second effect on the observed flux error that causes it to have a very complicated dependence was the small-scale modulation, which is caused by lower sensitivity at the overlapping higher Echelle orders of the spectrograph. We did not model such a small-scale variation in our mock catalogues, since our error estimates on both mock and real data would average over such small scales.

It should be noted that while the synthetic data in this paper were designed for analysis of the flux power spectrum, they should be applicable to other flux statistics as well.

3 DATA ANALYSIS

In this section, we describe the steps taken in the data analysis procedure. The same strategy was adopted for both real and synthetic data in order to check for any systematic effect arising due to the analysis itself.

The bulk of the analysis consists of the Fourier transforms of the input spectra, which is a method that has been used extensively before, on similar data sets (Croft et al. 1999, 2002; Kim et al. 2004; Viel et al. 2004, 2013a). This method is used to measure the flux power spectrum of the Lyα forest. The measurements, of both real and synthetic data, are in 7 z−bins ($z = 3.0$–4.2 with step $\Delta z = 0.2$) and 19 k−bins ($k = 0.003$–0.06 km^{-1} s, linearly binned with step $\Delta k = 3 \times 10^{-3}$ km^{-1} s).

3.1 Continuum

Using the provided continuum fits for each QSO spectrum (C), we first divided the continuum of the XQ-100 spectrum measurement (f). While we tested the robustness of the results by using different continuum models, we opted in the end for the official XQ-100 continuum fits described in López et al. (2016). We did not fit the continuum at the same time as the mean flux or the power spectrum. In the synthetic data, the continuum was modelled as a constant equal to unity.

3.2 Redshift sub-samples

For each line of sight, we split the data into separate sub-samples (z-bins) by measured redshift. Each pixel is assigned an absorption

redshift that determines the redshift of the sub-sample it falls into. We perform this step, so that the Fourier Transform used for the power spectrum analysis is performed on the level of z-bins and not on the whole line of sight. This is foremost much easier to handle, since the scales of different mean redshifts are not mixed together. It is also convenient to measure the power within a redshift bin where the variation in wavelength is described by a velocity coordinate only. This is an approximation, since measuring flux along a photon's path gives a relation between redshift and proper coordinate (or equivalently velocity coordinate). However, the corrections are very small when measuring Lyα power spectrum (McDonald et al. 2006; Iršič, Di Dio & Viel 2016).

3.3 Mean flux

We perform an un-weighted average of the flux to obtain an estimate of the mean flux ($\bar{F} = \langle F \rangle = \langle f/C \rangle$). A sample average gives us an unbiased estimator of the true value, but underestimates the error on the average. To perform the unbiased weighted average, the full variance would have to be known (which is the sum of the error flux variance and variance due to cosmic fluctuations). However, the cosmic variance is not known at this stage in the data analysis. One option would be to measure the mean flux and its variance together through a likelihood-based iteration scheme, or compute the variance from the measured power spectrum. We opted for the latter and simpler method.

3.4 Flux power spectrum

For each line of sight, and each z-bin we perform Fourier Transform on a flux fluctuation field ($\delta_F = F/\bar{F} - 1$). The flux power estimator is then given as a sum of the squared Fourier coefficients over all the pixels in all the z-bins along all the lines of sight that contribute to the measured (k, z) bin:

$$\hat{P}_{\rm tot}(k_i, z_j) = \frac{1}{N_{ij}} \sum_{n,m} |\delta_F(k_n, z_m)|^2 \delta_D(k_i - k_n)\delta_D(z_j - z_m), \quad (2)$$

where N_{ij} represents the number of pixels contributing to the bin (k_i, z_j). The sum goes over all the pixel pair configurations with a wavenumber k_n and redshift z_m. We have denoted the Dirac delta function as δ_D.

At this point, we also correct the result for the effects of finite pixel width and resolution element. Deconvolution of the flux fluctuation field translates into simple division in the Fourier space, thus

$$\delta_F(k_n, z_m) = \frac{\delta_F^{\rm (measured)}(k_n, z_m)}{W^2(k_n; p_{n,m}, R_{n,m})}, \quad (3)$$

where $p_{n, m}$ is pixel width of pixel corresponding to bin (k_n, z_m) and $R_{n, m}$ is resolution element of the same pixel. Both p and R are in velocity units. The pixel width p is constant in both our data sets ($p = c\Delta\log_{10}\lambda$, with λ in Å), whereas the resolution element can vary and is given for each pixel. In the synthetic data set, R is constant and equal to 33 km s^{-1} but in the real data set it varies between 11 and 20 km s^{-1} due to different resolutions in different spectral arms.

The de-convolution kernel in Fourier space, $W(k; p, R)$, is a product of a Gaussian (Gaussian smoothing of the resolution element) and a Fourier transform of a square function (pixel width):

$$W(k; p, R) = e^{-\frac{1}{2}k^2 R^2} \frac{\sin^2\left(\frac{kp}{2}\right)}{\left(\frac{kp}{2}\right)^2}. \quad (4)$$

3.5 Noise power

In the subsection above, we have explained how the total flux power spectrum is evaluated. However, this power describes both fluctuations due to noise and the cosmological signal we are interested in. It is fair to assume that noise is uncorrelated with the cosmological signal, and thus it can be removed at the power spectrum level:

$$P_F(k, z) = P_{\text{tot}}(k, z) - P_N(k, z). \tag{5}$$

We estimate the noise power by assuming that the $P_N(k, z)$ can be treated as constant in k, and its normalization for each redshift can be obtained through the variance of the flux errors as a function of redshift. To that end, we compute the estimate of the flux error variance, at the step when we compute the mean flux

$$\sigma_N^2(z_j) = \sum_i \frac{\sigma_F^2(\lambda(z_i))}{M_j}, \tag{6}$$

where M_j is the number of pixels that correspond to a redshift bin z_j. The noise power is then given by

$$\bar{F}^2(z)\sigma_N^2(z) = \frac{1}{\pi} \int_0^\infty P_N(k, z)\, dk \approx \frac{1}{\pi} P_N(z)(k_{\max} - k_{\min}), \tag{7}$$

where $k_{\min} = 0$ for our choice of binning and $k_{\max}$ is equal to Nyquist scale, which is the largest independent scale we measure through our Fourier Transform analysis.

The estimate obtained through the above relation is used in our data analysis as the noise power. This method has been tested on synthetic data (see the next section) and provides satisfactory results.

4 RESULTS

In this section, we present the results of the data analysis procedure presented in this paper. First, we show the results and tests of various methods and approximations used in the analysis of the synthetic data. We then show the main results of this paper, performed on the XQ-100 sample of QSO spectra. In the last subsection, we discuss the way to obtain the estimate of the errors on the flux power spectrum bins.

4.1 Power spectrum results on synthetic data

First, we apply the data analysis procedure to the synthetic catalogue 5000 QSO spectra in order to test for possible systematic effects in our analysis. By using a larger number of QSO spectra, we hope to beat down the statistical fluctuations and proclaim the deviations that remain as systematic errors.

The measurements of the mean flux on synthetic data are presented in Fig. 3. The input mean flux with which we have calibrated the simulation outputs is plotted in full black line (BOSS 2013 – Palanque-Delabrouille et al. 2013). Red points with error bars are measurement from the data analysis procedure presented in this paper. The results agree well with the input version and suggests no important systematic effects are present in this measurement. The analysis was also repeated on a synthetic catalogue with only 100 QSOs. The results are plotted in green in Fig. 3, and agree well with the 5000 QSO spectra sample. Note however that the error bars are very similar, and that is because they are dominated by the variance of flux fluctuations. As a comparison, Fig. 3 also shows observed flux from two other surveys (Kim et al. 2007 and Becker et al. 2013; Viel et al. 2013a) on a different sample of measured real data spectra.
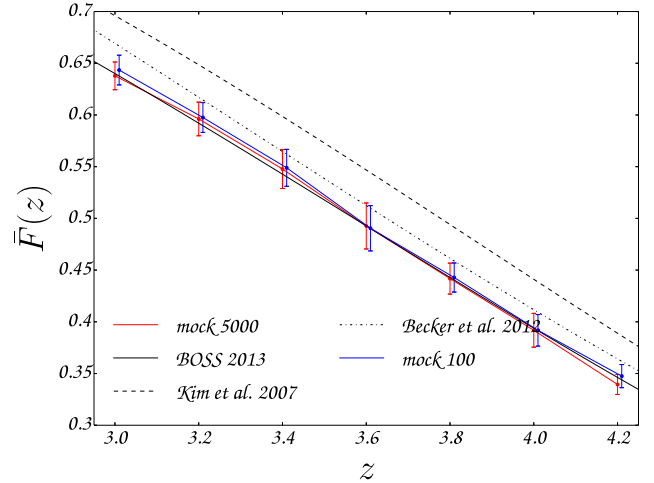

Figure 3. The mean transmitted flux as obtained from the synthetic data. In red, we show results using 5000 mock QSO spectra and using 100 mock QSO spectra (in blue). In black, we plot the standard observational results by Kim et al. (2007, dashed), Becker et al. (2013, dot–dashed) and Palanque-Delabrouille et al. (2013, full line). The input to the mocks was the BOSS mean flux. The data points are shifted in redshift (by 0.01) to be readily distinguishable.
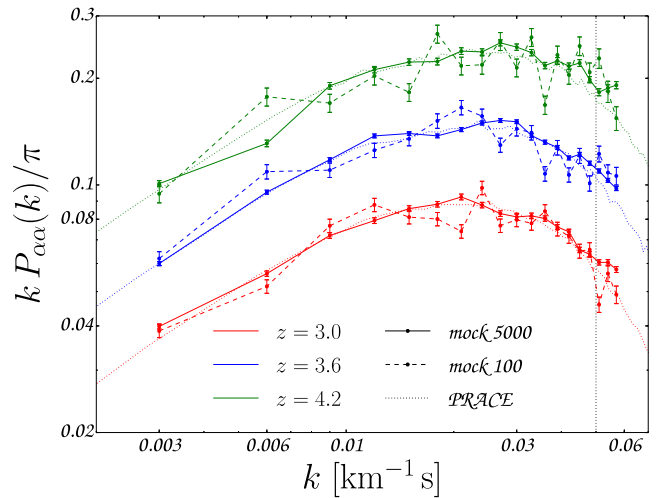

Figure 4. The flux power spectrum measured on the synthetic data for 5000 (full lines) and 100 (dashed lines) QSO spectra is shown. The three colours correspond to three (out of seven measured) redshift bins: $z = 3.0$ (red), $z = 3.6$ (blue) and $z = 4.2$ (green). The dotted lines correspond to the power spectrum extracted from a simulation at that redshift. The error bars are evaluated using bootstrap method (see Section 4.4 for details).

Next, the data analysis was tested on the measurements of the flux power spectrum. Fig. 4 shows the results as a function of scale (k) for three redshift bins ($z = 3.0$ – red, $z = 3.6$ – blue and $z = 4.2$ – green). The full lines represent the measurements performed on the synthetically generated spectra as described in Section 2.2. For comparison, we show the flux power spectrum obtained by measuring it directly on the simulation output at the specified redshifts (using 5000 lines of sight), without going through the construction procedure of the synthetic data (dotted lines). The departures from the input power spectrum at large scales are due to insufficient number of lines-of-sight probing those scales. This is
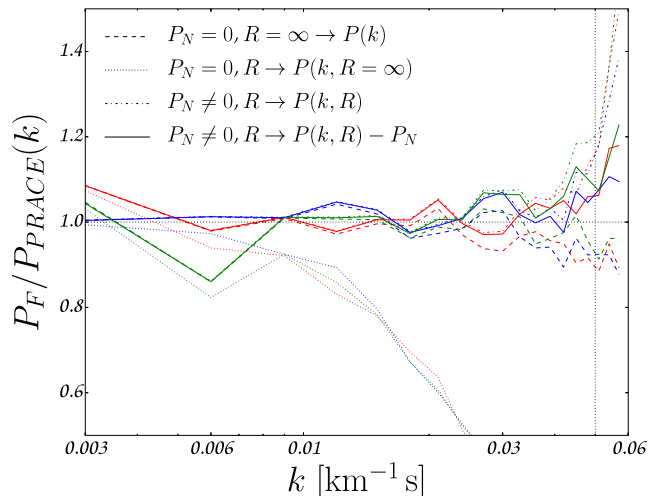
Figure 5. The ratio between flux power spectrum measured from the synthetic data (mock 5000) and the input simulation power spectrum is reported. The colours again correspond to three redshift bins (red – $z = 3.0$, blue – $z = 3.6$ and green – $z = 4.2$). Different line styles correspond to different assumptions when generating synthetic data as well as different data analysis steps taken: P_N – whether noise is added to the synthetic data, R – whether resolution/pixel width were added; $P(k, R)$ – whether in the data analysis resolution was corrected and $-P_N$ whether noise was subtracted (see the text for details).

apparent from looking at the dashed line in Fig. 4, where the same analysis is performed on only 100 QSO spectra.

However, there are still some fluctuations present at smaller scales that persist even when increasing the number of QSO spectra in our analysis of the synthetic data. Fig. 5 shows in greater detail the ratio between the recovered flux power from the synthetic data and simulation power spectrum at those redshifts. The three colours still represent three redshift bins, but different line style shows different tests done in either the construction of the mock data or the data analysis procedure.

The dashed coloured lines (Fig. 5) show the effect of not correcting for the pixel width. The lines show the recovered power spectrum from the mocks, where no noise has been added ($P_N = 0$) and no convolution with the resolution element has been performed ($R = \infty$). No corrections to noise, resolution or pixel width were added when extracting the flux power from the mocks. The ratio is different from unity because in the synthetic data the spectra were rebinned using XQ-100 wavelength bin size, while the flux power spectrum from simulations was computed using much finer binning.

The dotted lines (Fig. 5) show the effect of not correcting for the resolution element. The lines show the recovered power spectrum from the mocks with no noise ($P_N = 0$), but spectra were convolved with a Gaussian kernel with a resolution element R (see Section 2.2). However, no correction to the resolution was made in the data analysis. Comparing with dashed lines, properly correcting for the resolution has much bigger impact on the recovered flux power than correcting for the pixel width.

Additional tests were performed, where both noise ($P_N \neq 0$) and resolution (R) were added to the synthetic data, and while the data analysis corrected for the resolution element, no correction to the noise was added (dot–dashed coloured lines in Fig. 5). Not correcting for the noise clearly introduces spurious power on small scales that increases rapidly, while large scales remain unaffected.

The last test (full lines in Fig. 5) shows the effect of correcting the resolution element with slightly wrong value. We assume that our
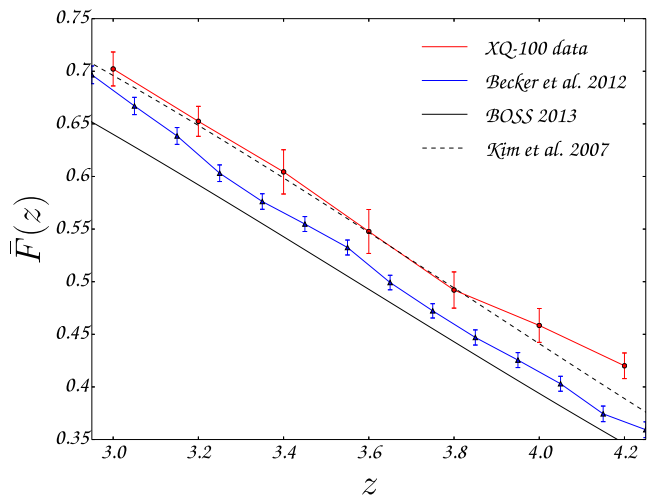

Figure 6. The mean transmitted flux measured on the XQ-100 data sample (red points) using the data analysis and cuts as described in Sections 3 and 2.1. As a comparison, we also plot results for mean flux from Palanque-Delabrouille et al. (2013, full black line) and extrapolated values from Kim et al. (2007, dashed black line). The error bars on the mean flux were taken to be from the bootstrap covariance matrix. We also compare our results to the mean flux measurements by Becker et al. (2013, blue points). The difference comes from different continua estimation (see the text for details).

knowledge of the (synthetic) data resolution element is of the order of few $km\,s^{-1}$ (or roughly 10 per cent). Both noise and XQ-100 pixel width were used in the construction of the mock sample, and both were as well corrected for in the power spectrum estimation. However, the effect of misestimating the resolution element translates into wrong power spectrum recovery on small scales. Deviations of the flux power spectrum on small scales ($k \sim 0.05\,km^{-1}\,s$) are of order of 5–10 per cent.

On large scales, tests agree nearly perfectly with each other, which indicates that the fluctuations there are specific to the data set not the data-analysis routine, and thus of statistical nature. However, on smaller scales the difference to the simulation power is interpreted as correcting for slightly wrong values of resolution element or pixel width (where resolution carries more weight). The differences are again of the same order of magnitude (5–10 per cent) at the small-scale end of our measurements. Additional cause of these differences might be that no correction has been made in the analysis regarding the aliasing of small scales approaching Nyquist scale. To account for these systematic effects in our data analysis, we use the results shown in full lines in Fig. 5 to determine the systematic errors. The absolute difference between the models shown in Fig. 5 (full lines) and the reference line of unity was used as a systematic error standard deviation.

4.2 Lyman α flux power spectrum from XQ-100 sample

This section contains the main results of the data analysis of the XQ-100 data sample. First, we present the measurements of the mean transmitted flux as a function of redshift, in Fig. 6. The error bars were obtained using the method described in Section 3.3. As a comparison, we also plot mean flux fitting formulas from Palanque-Delabrouille et al. (2013) and Kim et al. (2007). The mean flux measurements of XQ-100 data agree well with Kim et al. (2007) up to redshift around 3.8. The line for Kim et al. (2007) plotted in this paper is in fact an extrapolation of the fitting formula performed on lower redshift QSO spectra ($z < 3$). However, comparing it to
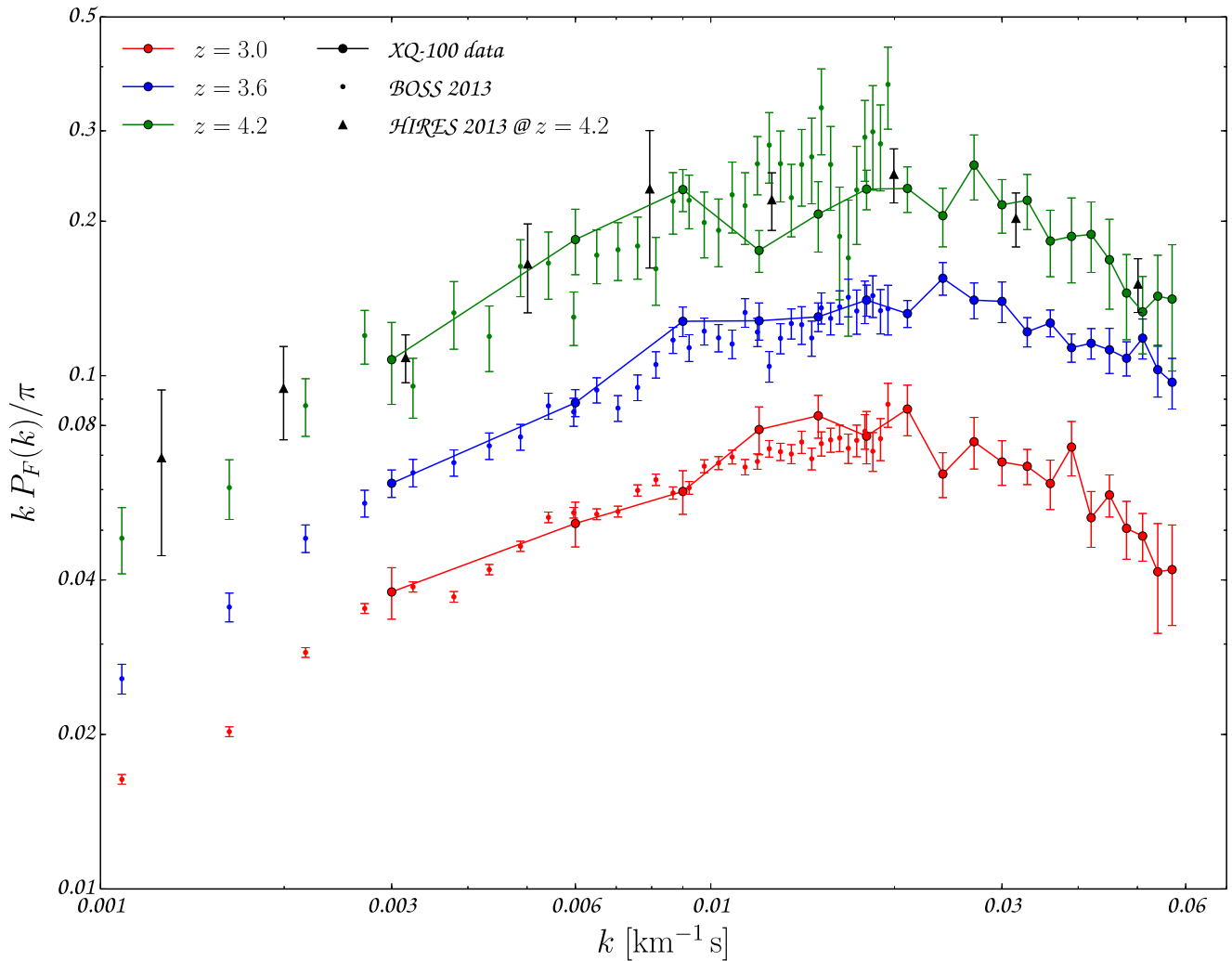
Figure 7. The flux power spectrum measurements of the XQ-100 data sample (circles). Full data analysis procedure described in Section 3 was applied, as well as all the cuts to the data presented in Section 2.1. We have also subtracted the metal power spectrum (see Section 4.3). The error bars used in this plot are a squared sum of both statistical errors (from bootstrap matrix estimation) and systematic errors (see Section 4.1). As a comparison measurements from Palanque-Delabrouille et al. (2013, dots) and Viel et al. (2013a, black triangles) are also plotted.

our results, it seems to be valid even at higher redshifts. The difference in mean flux normalization between our results and Palanque-Delabrouille et al. (2013) is probably due to different continuum fitting procedures. In Fig. 6, we also compare to the results of the mean transmitted flux of Becker et al. (2013). The difference is mainly due to different continuum fitting. Moreover, the results by Becker et al. (2013) presented in this paper were rescaled to match lower redshift measurements by Faucher-Giguère et al. (2008). Our data lack the sufficiently low redshifts ($z = 2$–2.5) to be used as rescaling of the results by Becker et al. (2013).

The most important result of our paper is present in Fig. 7. The figure shows the flux power spectrum, measured on the XQ-100 sample of QSO spectra, as a function of scale for three redshift bins from our analysis. All the steps from the data analysis procedure were performed in order to obtain the flux power values presented in this plot (see Table A1 for full sample of measurements). We have also subtracted the metal power spectrum, measured within the same data sample and extrapolated to lower redshifts (see Section 4.3). As a comparison, the measurements of the BOSS 2013 analysis are also plotted (Palanque-Delabrouille et al. 2013) as well

as overlapping redshift from high-redshift measurements (Becker et al. 2013). Since XQ-100 data sample only has 100 QSO spectra, the flux power cannot be measured at scales as large as BOSS analysis could. However, as predicted, due to higher resolution and signal to noise, smaller scales are measured. The error bars of the flux power used in this plot were estimated using a bootstrap covariance matrix of the data itself (see Section 4.4 for details) as well as the systematic errors estimation using the method described in Section 4.1. The XQ-100 flux power spectrum measurements presented in this paper also agree remarkably well with the high-redshift measurements.

4.3 Metal flux power spectrum

The flux power spectrum measured in this paper using the data analysis presented in Section 3 contains the power coming from both Lyα forest (predominantly) as well as a small contamination from the metals.

Typically one can estimate the metal power spectrum in the QSO spectra redwards of the Lyα emission line, where only metal
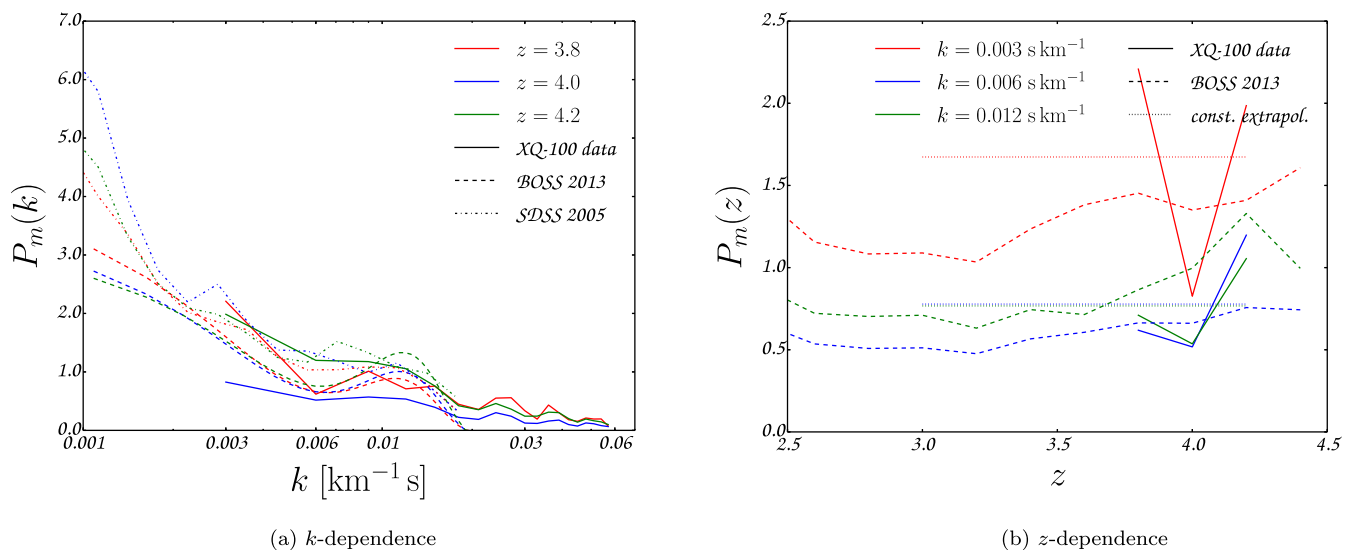
(a) *k*-dependence

(b) *z*-dependence

Figure 8. (a) The metal power spectrum measured in the restframe redshift range of 1268–1380 Å for three redshift bins: $z = 3.8$ (red), $z = 4.0$ (blue) and $z = 4.2$ (green). Measurements of metal power spectrum by McDonald et al. (2005, dot–dashed lines) and Palanque-Delabrouille et al. (2013, dashed lines) are also plotted. (b) The measurements of the metal power spectrum as a function of redshift, for three different *k*-modes: $k = 0.003\,\mathrm{km^{-1}\,s}$ (red), $k = 0.006\,\mathrm{km^{-1}\,s}$ (blue) and $k = 0.012\,\mathrm{km^{-1}\,s}$ (green). The dashed lines show the result by Palanque-Delabrouille et al. (2013). Previous measurements of metal power (dashed lines) indicate that the redshift dependence can be approximated as roughly constant for each *k*-mode. Dotted lines show our result of such an approximation, which is also used to extrapolate $P_m(k, z)$ to lower redshift bins.

absorption is present (McDonald et al. 2005). The absorption due to metals is coming from mostly lower redshifts, but if unidentified it contaminates the higher redshift Lyα forest. It is thus further assumed that the metal fluctuations are uncorrelated with the real Lyα signal, and that one can remove the effect of the metals by subtracting their power spectrum from the measured one. If higher accuracy is desired, further corrections can be added to this approach (Iršič & Slosar 2014).

However, to measure the power spectrum redwards of the Lyα emission line, *for the same redshift range*, where flux power in the forest is measured, a secondary sample of lower redshift QSO spectra is needed. Since XQ-100 data sample contains only 100 quasars at relatively high redshift, measurements of the metal power spectrum could only be achieved for the higher redshift bins, as shown in Fig. 8(a). To measure the power, we have adopted the restframe wavelength range of 1268–1380 Å in each QSO spectrum. As is evident from Fig. 8(a), the results are slightly noisy compared to the metal power estimated in Palanque-Delabrouille et al. (2013).

To estimate the Lyα forest flux power for all redshifts, we have performed a simple extrapolation of the metal power spectrum measurements. For each *k*-bin, the value of metal power remains roughly constant as a function of redshift in the measurements of Palanque-Delabrouille et al. (2013). Using this information, we averaged our $P_m(k, z)$ over the three redshift measurements for each *k*-bin and used this as an extrapolation to lower redshifts. This is shown in Fig. 8(b). Even though such an approximation is very rough, the value of $P_m(k, z)$ is generally smaller or at best of the same order as the statistical errors on our flux power spectrum measurements.

To perform a more detailed analysis of the metal power spectrum, another sample of lower redshift quasars would be needed, or individual metals contaminating the forest would need to be identified. However, we believe that the results would not change significantly and leave such a detailed analysis for future studies.

4.4 Covariance matrix

To estimate the error bars on the flux power spectrum, the separate QSO spectra contributions to the power spectrum were bootstrapped by assuming each spectrum to be an independent measurement of the flux power (Slosar et al. 2011, 2013; Iršič et al. 2013). We generated 1000 bootstrapped samples of the input data set and calculated the corresponding bootstrap covariance matrix.

The method was applied first to the synthetic data sample, for mean flux as well as flux power spectrum measurements. Fig. 9(a) shows how the diagonal elements of the bootstrapped covariance matrix (bootstrap variance) for the mean flux change as a function of redshift. The relative error on the mean flux from bootstrapped samples is roughly constant. Different line styles correspond to using 100 or 1000 bootstrap samples, and the differences are small. Two colour schemes (magenta and green) correspond to estimating the error bars on a mock 100 or 5000 catalogues. The ratio between the two estimations is exactly $\sqrt{N_Q(\mathrm{mock}\ 5000)}/\sqrt{N_Q(\mathrm{mock}\ 100)}$, meaning that the variance scales as expected with the number of QSO spectra in the sample ($\sim 1/\sqrt{N_Q}$). In red, we plot the estimates of the mean flux error bars coming from the integrals over the full (signal + noise) power spectra at each redshift bin.

Same analysis test was performed also on the flux power spectrum variance estimation, as shown in Fig. 9(b). Full lines and dot–dashed lines correspond to the bootstrapped samples of mock 100 and mock 5000 QSO spectra, respectively. The scaling of the variance holds in this case as well. In dashed lines, we show the estimation of the systematic errors on the mean flux (see Section 4.1).

The full bootstrap covariance matrix of the flux power spectrum is shown in Fig. 10. The plots correspond to the analysis done on mock 5000 (Fig. 10a) and mock 100 (Fig. 10b) synthetic quasar catalogues. The covariance matrix in the plots was normalized (i.e. what is shown is $C_{ij}/\sqrt{C_{ii}C_{jj}}$) so that the structure is readily discernible. Within one redshift bin the correlations between different k-bins are largely uncorrelated, with small correlation growing from large to small scales. However, the correlations between adjacent
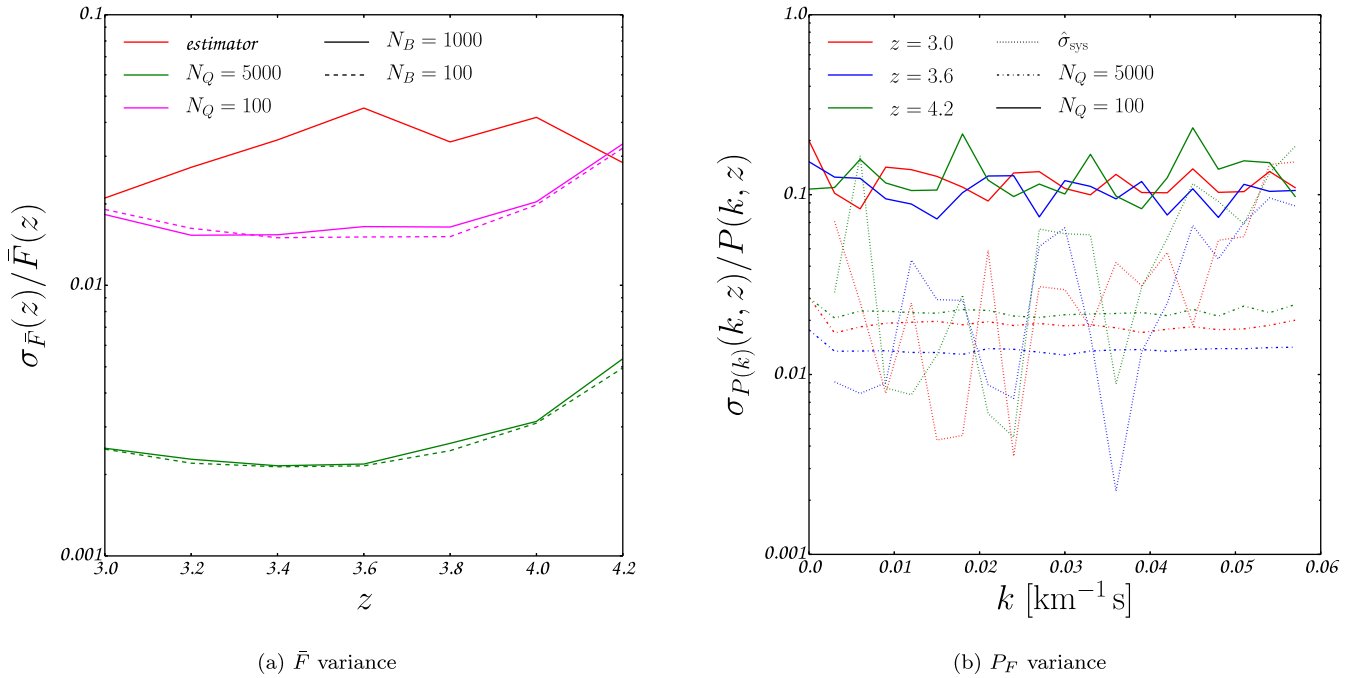
(a) $\bar{F}$ variance

(b) P_F variance

Figure 9. (a) The estimation of relative variance on the mean flux measurements of the synthetic data sample. In red is shown the variance obtained through our data analysis (see Section 3.3), while magenta and green colours present the 1000 bootstrapped variance of mock 100 and 5000 QSO spectra sample, respectively. Dashed lines show the corresponding variance when only 100 bootstrap samples were used. (b) The estimation of the relative variance on the flux power spectrum measurements of the synthetic data sample. Three colours correspond to three redshift bins: red – $z = 3.0$, blue – $z = 3.6$ and green – $z = 4.2$. Full and dot–dashed lines show the results obtained on mock 100 and 5000 QSO spectra samples, respectively (both with 1000 bootstrap samples). In dotted lines, the estimation of the systematic error is shown.
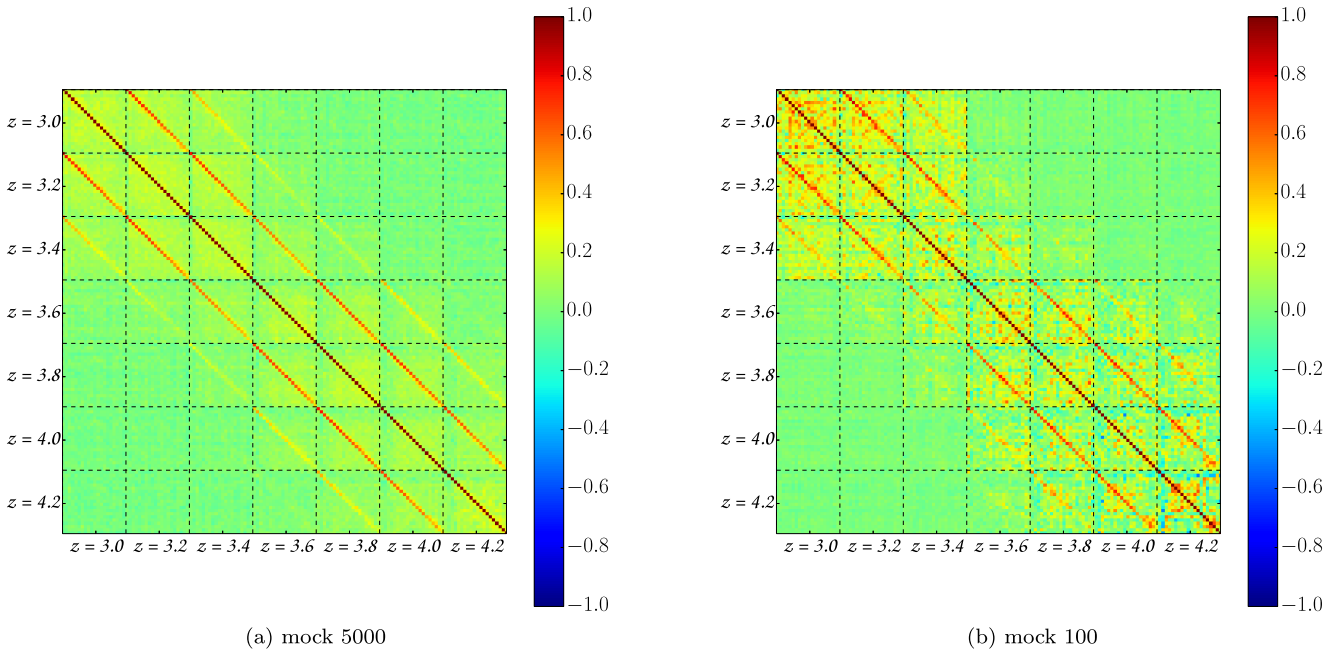

(a) mock 5000

(b) mock 100

Figure 10. The error correlation matrices of the flux power spectrum ($C_{ij}/\sqrt{C_{ii}C_{jj}}$). Fig. (10a) corresponds to the analysis done on 5000 synthetic spectra, and Fig. (10b) to the analysis on only 100 synthetic spectra. The structure of the plot is that within each labelled redshift bin, the k-bins follow in increasing order. See the text for details.

redshift bins are quite large. This is a spurious result of the way synthetic data are generated since up to two simulation snapshots with successive redshift span roughly the size of one redshift bin in the measurements. The structure remains basically the same (albeit

noisier) when comparing the results obtained on only a 100 QSO spectra.

Finally, the same scheme was adopted on the XQ-100 sample, and the results of the bootstrap covariance matrix are shown in
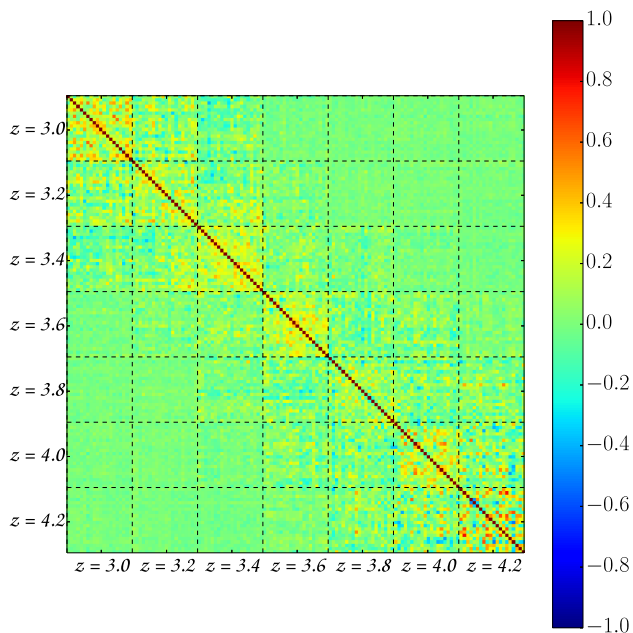
Figure 11. The error correlation matrix ($C_{ij}/\sqrt{C_{ii}C_{jj}}$) of the flux power spectrum measurements of the XQ-100 sample. See the text for details.

Figure 12. This figure shows the levels of the leaking continuum power spectrum into the total measured Lyα forest power spectrum (dot–dashed lines). Compared to the statistical (and systematic) errors evaluated in the previous sections of this paper (dashed lines), uncertainties due to continuum fitting are small on the measurements of the power spectrum. The full forest flux power and the power spectrum of the noise are shown as a comparison (full lines and dotted lines, respectively). The three colours represent three redshift bins: $z = 3.0$ (red), $z = 3.6$ (blue) and $z = 4.2$ (green).

Fig. 11. The correlation matrix is somewhat noisy, which is to be expected comparing to the analysis with the varying number of input spectra performed on the synthetic data. The correlations with adjacent redshift bins are negligible.

Previous studies have shown that bootstrapped covariance matrix underestimates the variance elements of the matrix by roughly 10 per cent (Kim et al. 2004; Busca et al. 2013; Iršič et al. 2013; Palanque-Delabrouille et al. 2013; Slosar et al. 2013). To compensate for that in order to achieve a conservative estimation of the error bars, the full bootstrapped covariance matrix was multiplied by a factor of 1.1.

4.5 Continuum errors

Since the absorption of the IGM at higher redshift becomes stronger, it becomes hard to provide an objective estimate of the continuum levels, due to inability to find transmission regions in the Lyα forest. Most attempts in the literature regarding this issue assume that either the quasar intrinsic emission in the Lyα forest region is unchanging from quasar to quasar and with redshift, or they model it on a quasar-by-quasar basis (Kim et al. 2004; McDonald et al. 2005; Busca et al. 2013; Iršič et al. 2013; Palanque-Delabrouille et al. 2013; Slosar et al. 2013; Viel, Schaye & Booth 2013b).

Nevertheless, the discussions and analysis on the topic in the literature agree that a change in the normalization of the continuum level in the Lyα forest is perfectly degenerate with the mean transmitted flux estimations. On the other hand, any large-scale modulations of the continuum affect the measurements of the correlations within the forest, but when working in Fourier space, they are confined to large scales.

To estimate the possible contamination of the continuum power leaking into the flux power spectrum, we perform a measurement of the bare continuum fits, as if they were representing fluctuating absorption features of the Lyα forest. This would be equivalent to averaging the continua over all the lines of sight, to obtain an average and a statistical description of its fluctuations. Such an ap-
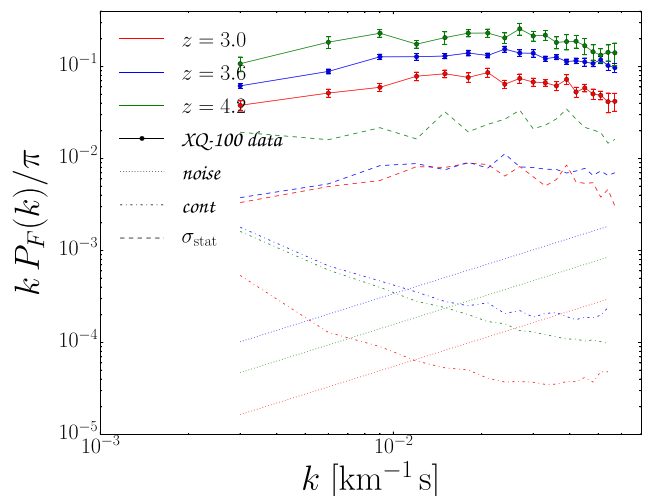
proach is a valid approximation in the limit for which we assume that all quasar continua follow the same shape (but different normalization due to different overall observed fluxes). The results of this simple model are shown in Fig. 12. The figure shows the continuum power spectra for three different redshift bins (dot–dashed line), compared to the levels of the statistical errors (dashed line) on the measurements of the flux power (full line).[1] The continuum power spectra show a plateau-like feature towards smaller scales ($k > 0.01$ km^{-1} s), increasing in power towards large scales ($k < 0.01$ km^{-1} s), as expected from previous analysis. The level of the continuum power leaking into the total forest flux power is thus very small, indeed it is comparable to the estimated noise power (dotted line).

While we do not use this approach in our standard analysis, it convinces us that the systematic errors due to the continuum estimation that would result into increased uncertainties on very large scales are much smaller than the statistical and systematic errors on our measurements and can thus be neglected. We caution that this is a simple estimation, and valid only for the data presented in this paper.

5 CONCLUSIONS

In this paper, we have performed an Lyα flux power spectrum analysis on the XQ-100 sample of 100 medium resolution, medium signal-to-noise QSO spectra in the redshift range $3.5 < z < 4.5$ (López et al. 2016). The results are shown in Fig. 6 for the mean flux measurements, in Fig. 7 for the flux power spectrum measurements and in Fig. 11 for the estimation of the error correlations of the flux power.

The resulting mean transmitted flux is in good agreement with previously measured mean flux by Kim et al. (2007) at lower

---

[1] The systematic errors estimated in Section 4.1 are comparable to the statistical errors, and are not shown in this figure.

redshifts. The redshift dependence shows slight deviations from the fitting formula in the Kim et al. (2007) paper at the higher redshift end, but it is still within 1σ–2σ discrepancy.

Measurements of the flux power spectrum cover the range of $z = 3.5$–4.2 in seven redshift bins and $k = 0$–$0.06\,\mathrm{km}^{-1}\,\mathrm{s}$ in 20 k-mode bins. The results agree well with the expectations that despite a small sample of QSO spectra, the higher values of spectral resolution and signal-to-noise ratio allow for measurements of smaller scales than a large QSO number survey such as SDSS-III/BOSS (Dawson et al. 2013). The total error bars on our measurements (combined statistical and systematic) are of the same order as those in BOSS analysis, specifically on small scales ($k > 0.01\,\mathrm{km}^{-1}\,\mathrm{s}$). At higher redshifts ($z > 3.6$), our error bars are even smaller by more than 50 per cent.

In the final analysis, the official (and publicly available) XQ-100 Legacy Survey continuum fits were used. To consistently measure the mean flux (and flux power), a simultaneous measurement of the quasar continua should be performed. However, wrong estimation of the continuum levels would result in a slight change of normalization in the mean flux, while any long-range modulations of the continuum are absorbed into large-scales k-bins in the $P_F(k)$ measurements – and thus will not change the results on the medium to small scales this experiment probes.

Since many QSO spectra in the sample feature a DLA, these strong absorption system affect the flux power. In the current analysis, we have simply removed the pixels within 1.5 of the DLA equivalent width around the DLA central absorption redshift. However, with a more careful analysis DLA component could be removed from the spectra and thus additional wavelength ranges could be potentially added to the flux power spectrum analysis to increase the final signal to noise in the $P_F(k)$ measurements. However, since the effect on the flux power seemed to be small and only affected large-scale k-bins, a simpler approach was adopted in the final analysis of the data.

Through the use of a realistic synthetic QSO spectra sample, an estimation of the systematic error of our data analysis was obtained. However, for the larger part the systematic error bars are below the statistical errors, obtained through bootstrapping the data sample. This is valid at least in the probed k-mode range. At larger scales, additional contribution to systematic errors is introduced due to imperfect continuum fitting, while at small scales imperfect deconvolution of the resolution/pixel width contribution introduces significant obstacles. Last but not least, a Fourier Transform analysis also introduces aliasing on small scales that is difficult to correct for. For that reason, such small scales (just below Nyquist k-mode) were not measured in the data analysis presented in this paper. We leave such corrections to subsequent analysis.

Due to lack of lower-redshift quasars in the XQ-100 sample, the contaminating metal power in the Lyα forest was only measured in three highest redshift bins ($z = 3.8$–4.2). A simple and rough extrapolation was used to obtain an estimate of the metal power at smaller redshifts. A separate study could be used to address this issue. We also point out that if the metal power spectrum is measured sufficiently accurately at all redshifts, additional second-order corrections are known to be necessary to recover the Lyα forest flux power (Iršič & Slosar 2014).

The results on the flux power spectrum presented in this paper have a great potential in putting additional constraints on the cosmological parameters, as the measurements stretch between large and small scales, probed respectively by low-resolution large-quasar number surveys, and a few high-resolution, high signal-to-noise QSO spectra. The power in these intermediate scale range is sensitive to the small-scale properties of the dark matter, as well as to reionization epoch through the Jeans scale measurements.

REFERENCES

Becker G. D., Bolton J. S., Haehnelt M. G., Sargent W. L. W., 2011, MNRAS, 410, 1096

Becker G. D., Hewett P. C., Worseck G., Prochaska J. X., 2013, MNRAS, 430, 2067

Bi H., Davidsen A. F., 1997, ApJ, 479, 523

Boera E., Murphy M. T., Becker G. D., Bolton J. S., 2014, MNRAS, 441, 1916

Bolton J. S., Viel M., Kim T.-S., Haehnelt M. G., Carswell R. F., 2008, MNRAS, 386, 1131

Bolton J. S., Becker G. D., Raskutti S., Wyithe J. S. B., Haehnelt M. G., Sargent W. L. W., 2012, MNRAS, 419, 2880

Bolton J. S., Puchwein E., Sijacki D., Haehnelt M. G., Kim T.-S., Meiksin A., Regan J. A., Viel M., 2017, MNRAS, 464, 897

Busca N. G. et al., 2013, A&A, 552, A96

Cen R., Miralda-Escudé J., Ostriker J. P., Rauch M., 1994, ApJ, 437, L9

Croft R. A. C., Weinberg D. H., Pettini M., Hernquist L., Katz N., 1999, ApJ, 520, 1

Croft R. A. C., Weinberg D. H., Bolte M., Burles S., Hernquist L., Katz N., Kirkman D., Tytler D., 2002, ApJ, 581, 20

Dawson K. S. et al., 2013, AJ, 145, 10

Faucher-Giguère C.-A., Prochaska J. X., Lidz A., Hernquist L., Zaldarriaga M., 2008, ApJ, 681, 831

Garzilli A., Bolton J. S., Kim T.-S., Leach S., Viel M., 2012, MNRAS, 424, 1723

Gunn J. E., Peterson B. A., 1965, ApJ, 142, 1633

Hernquist L., Katz N., Weinberg D. H., Miralda-Escudé J., 1996, ApJ, 457, L51

Hui L., 1999, ApJ, 516, 519

Iršič V., Slosar A., 2014, Phys. Rev. D, 89, 107301

Iršič V. et al., 2013, J. Cosmol. Astropart. Phys., 9, 16

Iršič V., Di Dio E., Viel M., 2016, J. Cosmol. Astropart. Phys., 2, 051

Kim T.-S., Viel M., Haehnelt M. G., Carswell R. F., Cristiani S., 2004, MNRAS, 347, 355

Kim T.-S., Bolton J. S., Viel M., Haehnelt M. G., Carswell R. F., 2007, MNRAS, 382, 1657

Lee K.-G. et al., 2015, ApJ, 799, 196

Lidz A., Faucher-Giguère C.-A., Dall'Aglio A., McQuinn M., Fechner C., Zaldarriaga M., Hernquist L., Dutta S., 2010, ApJ, 718, 199

López S. et al., 2016, A&A, 594, A91

Lynds R., 1971, ApJ, 164, L73

McDonald P. et al., 2005, ApJ, 635, 761

McDonald P. et al., 2006, ApJS, 163, 80

McQuinn M., 2016, ARA&A, 54, 313

Meiksin A. A., 2009, Rev. Mod. Phys., 81, 1405

Miralda-Escudé J., Cen R., Ostriker J. P., Rauch M., 1996, ApJ, 471, 582

Palanque-Delabrouille N. et al., 2013, A&A, 559, A85

Ricotti M., Gnedin N. Y., Shull J. M., 2000, ApJ, 534, 41

Rudie G. C., Steidel C. C., Pettini M., 2012, ApJ, 757, L30

Sánchez-Ramírez R. et al., 2016, MNRAS, 456, 4488

Schaye J., Theuns T., Rauch M., Efstathiou G., Sargent W. L. W., 2000, MNRAS, 318, 817

Slosar A. et al., 2011, J. Cosmol. Astropart. Phys., 9, 1

Slosar A. et al., 2013, J. Cosmol. Astropart. Phys., 4, 26

Theuns T., Zaroubi S., 2000, MNRAS, 317, 989

Theuns T., Leonard A., Efstathiou G., Pearce F. R., Thomas P. A., 1998, MNRAS, 301, 478

Theuns T., Zaroubi S., Kim T.-S., Tzanavaris P., Carswell R. F., 2002, MNRAS, 332, 367

Vernet J. et al., 2011, A&A, 536, A105

Viel M., Matarrese S., Mo H. J., Theuns T., Haehnelt M. G., 2002, MNRAS, 336, 685

Viel M., Haehnelt M. G., Springel V., 2004, MNRAS, 354, 684

Viel M., Lesgourgues J., Haehnelt M. G., Matarrese S., Riotto A., 2005, Phys. Rev. D, 71, 063534

Viel M., Becker G. D., Bolton J. S., Haehnelt M. G., 2013a, Phys. Rev. D, 88, 043502

Viel M., Schaye J., Booth C. M., 2013b, MNRAS, 429, 1734

Vogt S. S. et al., 1994, Proc. SPIE, 2198, 362

York D. G. et al., 2000, AJ, 120, 1579

Zhang Y., Anninos P., Norman M. L., 1995, Am. Astron. Soc. Meeting Abs., 1412

APPENDIX A: TABLE – MEASURED LYα FLUX POWER SPECTRUM

The last column $P_F(k, z)$ shows the total measured flux power spectrum, while the third column shows our estimate of the Lyα forest power spectrum $P_\alpha(k, z)$, where we have subtracted the extrapolated metal power spectrum. The second-to-last column is measured metal power spectrum, with a dash where no data could be measured within the XQ-100 data set. Statistical errors (σ_{stat}) were obtained using bootstrap covariance matrix on the data. The systematic errors were obtained through analysis on synthetic data (see Section 4.1). The flux power spectrum and its covariance matrix can be obtained from the following link: http://adlibitum.oats.inaf.it/XQ100survey/Data.html

Table A1. Measured Lyα flux power spectrum from XQ-100 data sample. All power spectrum (and error) columns are in [km s^{-1}] units. The scale k is in (km^{-1} s) units. The columns are: mean redshift and scale of the power spectrum bin, estimated Lyα forest flux power, measured metal and total flux power, as well as statistical and systematic errors.

z	k (km^{-1} s)	$P_\alpha(k, z)$ (km s^{-1})	σ_{stat} (km s^{-1})	σ_{sys} (km s^{-1})	$P_m(k, z)$ (km s^{-1})	$P_F(k, z)$ (km s^{-1})
3.0	0.003	39.6936	3.47799	2.96111	–	41.3668
3.0	0.006	26.9847	2.59723	0.740328	–	27.7626
3.0	0.009	20.7667	2.01472	0.197852	–	21.6864
3.0	0.012	20.5633	2.13739	0.518419	–	21.3302
3.0	0.015	17.4999	1.67476	0.077641	–	18.1371
3.0	0.018	13.3093	1.55476	0.0705116	–	13.6733
3.0	0.021	12.8818	1.28926	0.677582	–	13.1812
3.0	0.024	8.42079	0.843842	0.0403608	–	8.85882
3.0	0.027	8.65179	0.952071	0.297344	–	9.03964
3.0	0.03	7.11185	0.663833	0.251926	–	7.34621
3.0	0.033	6.34019	0.478553	0.14305	–	6.52495
3.0	0.036	5.38066	0.516292	0.293888	–	5.68213
3.0	0.039	5.84972	0.684576	0.190915	–	6.11011
3.0	0.042	3.9562	0.41663	0.263036	–	4.11763
3.0	0.045	4.0884	0.375191	0.0865709	–	4.21108
3.0	0.048	3.299	0.357229	0.232406	–	3.47645
3.0	0.051	3.00056	0.234432	0.217284	–	3.15771
3.0	0.054	2.41408	0.268641	0.517127	–	2.55463
3.0	0.057	2.30919	0.167658	0.483684	–	2.38873
3.2	0.003	50.5538	3.76044	3.48715	–	52.227
3.2	0.006	36.6106	2.45683	4.6167	–	37.3885
3.2	0.009	29.5313	1.86716	0.141733	–	30.451
3.2	0.012	23.1562	1.58399	0.42266	–	23.9231
3.2	0.015	17.56	1.14134	0.822192	–	18.1972
3.2	0.018	15.714	0.856297	1.42563	–	16.078
3.2	0.021	14.8417	1.04861	0.526579	–	15.1411
3.2	0.024	12.6287	1.02804	0.626563	–	13.0667
3.2	0.027	10.3106	0.762546	1.31213	–	10.6985
3.2	0.03	9.74955	0.807138	0.638237	–	9.98391
3.2	0.033	8.73696	0.571104	1.07065	–	8.92172
3.2	0.036	7.87109	0.607356	0.299586	–	8.17256

Table A1 – *continued*

z	$k \, (\mathrm{km^{-1}\,s})$	$P_\alpha(k, z) \, (\mathrm{km\,s^{-1}})$	$\sigma_{\mathrm{stat}} \, (\mathrm{km\,s^{-1}})$	$\sigma_{\mathrm{sys}} \, (\mathrm{km\,s^{-1}})$	$P_m(k, z) \, (\mathrm{km\,s^{-1}})$	$P_F(k, z) \, (\mathrm{km\,s^{-1}})$
3.2	0.039	7.55867	0.554116	0.14941	–	7.81906
3.2	0.042	6.41257	0.379081	0.193592	–	6.574
3.2	0.045	5.253	0.384992	0.0941316	–	5.37568
3.2	0.048	4.63914	0.336089	0.127258	–	4.81659
3.2	0.051	4.2735	0.306388	0.295822	–	4.43065
3.2	0.054	3.775	0.236653	0.220056	–	3.91555
3.2	0.057	3.25205	0.183355	0.281402	–	3.33159
3.4	0.003	54.6488	3.67166	1.31521	–	56.322
3.4	0.006	45.1101	2.37959	2.05999	–	45.888
3.4	0.009	33.6866	1.90515	1.59619	–	34.6063
3.4	0.012	29.4042	1.83353	1.34494	–	30.1711
3.4	0.015	22.2285	1.22494	0.165127	–	22.8657
3.4	0.018	21.4314	1.21646	1.31261	–	21.7954
3.4	0.021	18.3216	1.12336	0.561181	–	18.621
3.4	0.024	16.861	1.0669	0.458334	–	17.299
3.4	0.027	13.1393	0.752371	0.199968	–	13.5272
3.4	0.03	12.1581	0.747101	1.47473	–	12.3925
3.4	0.033	10.8306	0.739907	0.217761	–	11.0154
3.4	0.036	9.94063	0.65352	0.439429	–	10.2421
3.4	0.039	8.85191	0.541132	0.149585	–	9.1123
3.4	0.042	7.06202	0.441117	0.406511	–	7.22345
3.4	0.045	7.21777	0.520931	0.0199403	–	7.34045
3.4	0.048	6.5484	0.394166	0.0315864	–	6.72585
3.4	0.051	5.54113	0.357655	0.00463702	–	5.69828
3.4	0.054	5.33921	0.318303	0.279183	–	5.47976
3.4	0.057	4.79408	0.294146	0.180972	–	4.87362
3.6	0.003	64.6285	3.93553	0.572105	–	66.3017
3.6	0.006	46.3763	2.77871	0.391996	–	47.1542
3.6	0.009	44.561	2.92414	0.369775	–	45.4807
3.6	0.012	33.4982	2.30848	1.55865	–	34.2651
3.6	0.015	27.2763	1.57973	0.76344	–	27.9135
3.6	0.018	24.5006	1.58857	0.619505	–	24.8646
3.6	0.021	19.7668	1.17869	0.187915	–	20.0662
3.6	0.024	20.2644	1.47368	0.144347	–	20.7024
3.6	0.027	16.3306	0.943949	0.911005	–	16.7185
3.6	0.03	14.6182	0.837248	1.03125	–	14.8526
3.6	0.033	11.5936	0.729936	0.218077	–	11.7784
3.6	0.036	11.0542	0.663244	0.0259277	–	11.3557
3.6	0.039	9.13545	0.561005	0.137402	–	9.39584
3.6	0.042	8.65139	0.547743	0.221311	–	8.81282
3.6	0.045	7.84233	0.545822	0.572906	–	7.96501
3.6	0.048	7.07895	0.429794	0.330696	–	7.2564
3.6	0.051	7.29084	0.450913	0.471224	–	7.44799
3.6	0.054	5.97605	0.38174	0.574253	–	6.1166
3.6	0.057	5.35158	0.386213	0.466262	–	5.43112
3.8	0.003	94.9659	4.78048	3.15856	2.20798	97.1739
3.8	0.006	64.7637	5.17604	1.52262	0.618829	65.3825
3.8	0.009	51.1572	3.0288	0.770617	1.01263	52.1698
3.8	0.012	41.4319	3.02359	1.43161	0.710195	42.1421
3.8	0.015	35.5927	2.77421	0.320939	0.757387	36.3501
3.8	0.018	31.0847	2.22233	0.209592	0.44708	31.5318
3.8	0.021	26.1317	1.57351	0.170671	0.3575	26.4892
3.8	0.024	20.8432	1.57842	0.266877	0.55192	21.3951
3.8	0.027	18.3734	1.34587	0.00462213	0.558363	18.9318
3.8	0.03	15.6996	1.15623	0.621457	0.335736	16.0353
3.8	0.033	14.5548	0.924196	0.209155	0.192244	14.747
3.8	0.036	11.8421	0.884394	0.360085	0.433281	12.2754
3.8	0.039	10.5212	0.661361	0.370649	0.301957	10.8232
3.8	0.042	10.3815	0.811933	0.326826	0.18257	10.5641
3.8	0.045	9.4877	0.582263	0.466667	0.15454	9.64224
3.8	0.048	8.20416	0.531247	0.412172	0.211622	8.41578
3.8	0.051	6.52915	0.466894	0.355527	0.193798	6.72295
3.8	0.054	6.01328	0.467307	0.530194	0.195322	6.2086
3.8	0.057	5.25984	0.430496	0.592233	0.0734851	5.33333

Table A1 – *continued*

z	k (km^{-1} s)	$P_\alpha(k, z)$ (km s^{-1})	σ_{stat} (km s^{-1})	σ_{sys} (km s^{-1})	$P_m(k, z)$ (km s^{-1})	$P_F(k, z)$ (km s^{-1})
4.0	0.003	111.399	10.3519	3.8603	0.8259	112.225
4.0	0.006	68.0376	5.04346	2.3163	0.517393	68.555
4.0	0.009	52.8667	5.3455	1.82327	0.570465	53.4372
4.0	0.012	48.6669	4.45016	4.65906	0.535946	49.2028
4.0	0.015	41.833	3.42083	1.51375	0.394923	42.2279
4.0	0.018	29.9528	2.45372	0.581078	0.222861	30.1757
4.0	0.021	33.2897	2.75049	0.120818	0.18742	33.4771
4.0	0.024	28.6796	2.3593	0.771985	0.3025	28.9821
4.0	0.027	24.4995	2.33264	0.69748	0.242358	24.7419
4.0	0.03	21.8006	1.87943	0.592556	0.124732	21.9253
4.0	0.033	16.7224	1.48355	1.90312	0.118568	16.841
4.0	0.036	14.9103	1.3448	0.560797	0.159498	15.0698
4.0	0.039	14.4875	1.30919	0.113916	0.175863	14.6634
4.0	0.042	12.0117	1.05231	1.13926	0.0995424	12.1112
4.0	0.045	10.2184	0.786477	1.02756	0.0734334	10.2918
4.0	0.048	9.49697	0.662276	0.727909	0.126871	9.62384
4.0	0.051	8.66586	0.707745	0.91366	0.113339	8.7792
4.0	0.054	6.85466	0.612431	1.1111	0.0813378	6.936
4.0	0.057	7.21086	0.630264	1.21433	0.0649048	7.27576
4.2	0.003	112.535	20.2444	3.0241	1.98573	114.521
4.2	0.006	96.4383	8.39488	11.2881	1.19746	97.6358
4.2	0.009	80.4612	7.55641	0.560461	1.17602	81.6372
4.2	0.012	45.9185	4.27574	0.427649	1.05457	46.9731
4.2	0.015	43.2432	6.7416	0.597927	0.759341	44.0025
4.2	0.018	40.3104	3.4052	1.07437	0.421928	40.7323
4.2	0.021	34.65	3.52365	0.21666	0.353345	35.0033
4.2	0.024	26.8387	3.50562	0.139405	0.459671	27.2984
4.2	0.027	29.9342	3.90649	1.88457	0.362843	30.297
4.2	0.03	22.545	2.20596	1.55529	0.242615	22.7876
4.2	0.033	20.9133	2.19605	1.34463	0.243462	21.1568
4.2	0.036	15.9715	2.35841	0.167869	0.311622	16.2831
4.2	0.039	15.0499	2.78053	0.550652	0.303354	15.3533
4.2	0.042	14.0982	2.00849	0.926213	0.202175	14.3004
4.2	0.045	11.7465	1.52352	1.77379	0.140056	11.8866
4.2	0.048	9.48362	1.33956	1.18794	0.193858	9.67748
4.2	0.051	8.204	1.17976	0.772654	0.164307	8.36831
4.2	0.054	8.31223	0.855154	1.44071	0.144993	8.45722
4.2	0.057	7.77377	0.888949	1.9529	0.100243	7.87401

This paper has been typeset from a TEX/LATEX file prepared by the author.